r-PROCESS SITE(S) ?

[#1 ? in n' synthesis?]

- neutrino wind of the proto-neutron star in SN II/III/Ic
- decompression of neutron-rich material in neutron star binary merger

r-process is PRIMARY

~ SOLAR SYSTEM r-mix

→ no 'VARIABLES' at site

→ one site

SN II - ν DRIVEN WIND

- See Fig 1 / JANKA et al. 2007, Physics Reports

- IDEAS from NUCLEAR PHYSICS

T_9	Action items
≥ 10	n & p in NSE
~10	$n, p \rightarrow \alpha$ with n excess
~7	α + n excess
	$\alpha + \alpha + n \rightarrow {}^{9}Be$
	$^{9}Be(\alpha, n) \rightarrow {}^{12}C$
~5	NSE fails → α-process

A = 5, 8

$^{12}C(n,\gamma)^{13}C(\alpha,n)^{16}O(\alpha,n)^{20}Ne$

$\cdots \rightarrow \cdots \rightarrow$ A ~ 50-110 SEEDS

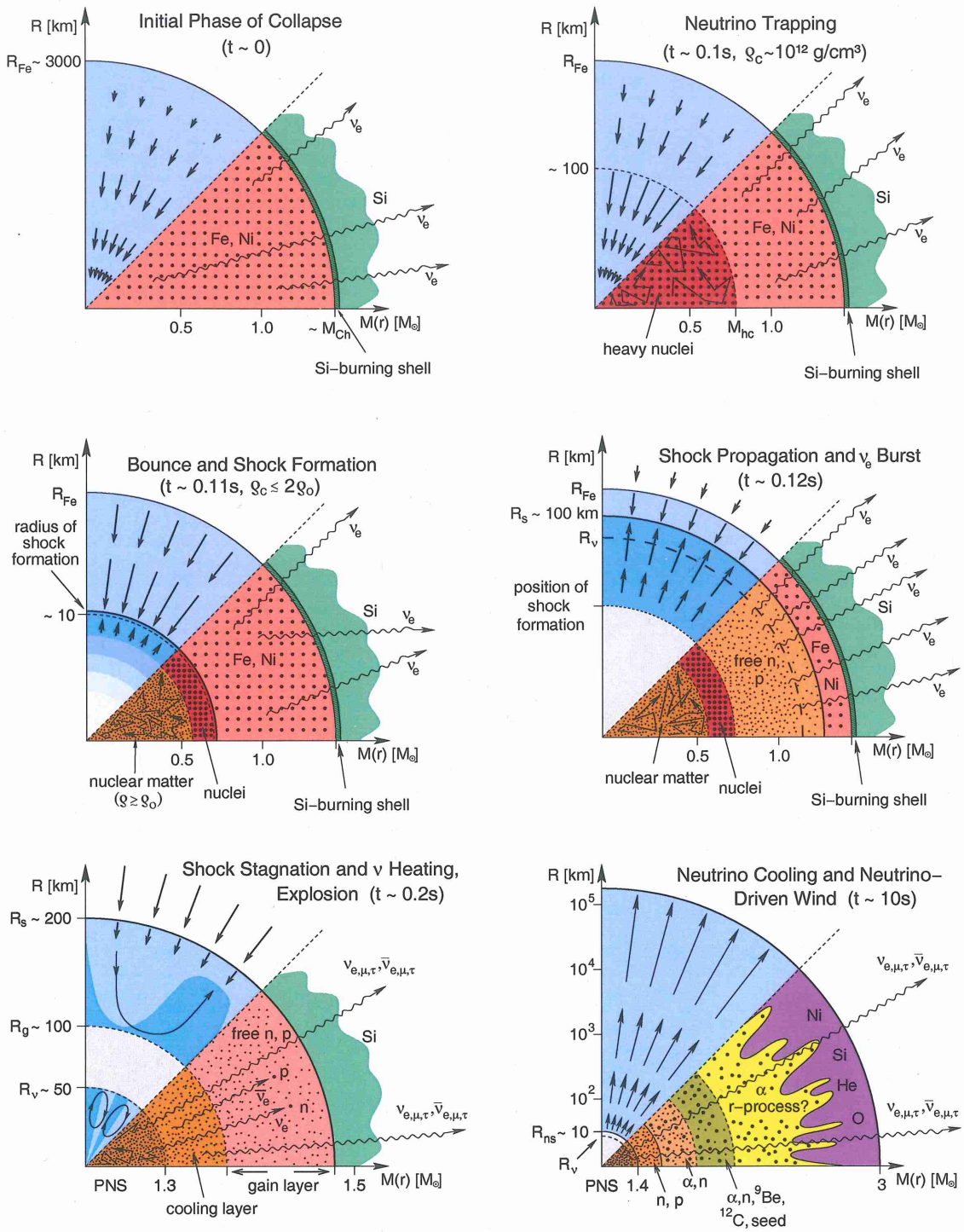

Figure 1: Schematic representation of the evolutionary stages from stellar core collapse through the onset of the supernova explosion to the neutrino-driven wind during the neutrino-cooling phase of the proto-neutron star (PNS). The panels display the dynamical conditions in their upper half, with arrows representing velocity vectors. The nuclear composition as well as the nuclear and weak processes are indicated in the lower half of each panel. The horizontal axis gives mass information. $M_{\rm Ch}$ means the Chandrasekhar mass and $M_{\rm hc}$ the mass of the subsonically collapsing, homologous inner core. The vertical axis shows corresponding radii, with $R_{\rm Fe}$, $R_{\rm s}$, $R_{\rm g}$, $R_{\rm ns}$, and R_ν being the iron core radius, shock radius, gain radius, neutron star radius, and neutrinosphere, respectively. The PNS has maximum densities ρ above the saturation density of nuclear matter (ρ_0).

JANKA et al.
Physics Reports 2007

~3 : α-process ceases
but IF
$n/SEEDS \sim 100$
→ STRONG r-PROCESS

≈ HIGH ENTROPY WIND
($S \sim 5.2\, T^3_{MeV}/\rho_8$)

BUT MODELS OF CORE COLLAPSE SN
→ LOW ENTROPY WIND
($n/SEEDS$ too low) (too slow)

CAN CONSTRUCT wind profiles
& do DYNAMIC calcs →
FIT SS MIX

PROBABLY EJECT SUFFICIENT MASS
& OCCUR FREQUENTLY

SOMETHING MISSING IN SN II MODELS ?

- EXPLOSIONS → EJECTA NOT ACHIEVED

Current supernova models (see, for example, Thompson, Burrows, and Meyer, 2001) give entropies of around 100 when what is needed to make the heaviest *r*-process nuclei is 300 to 400. The following possible solutions to this dilemma have been proposed (Qian and Woosley, 1996):

(a) the neutrino wind does not make all the solar *r* process, but only the lighter nuclei;
(b) there are extra energy inputs into the wind, such as magnetic fields, rotation, and shocks, that have been ignored and that might increase the entropy of the wind or decrease its time scale;
(c) the nuclear equation of state is very soft and the typical neutron star mass involved in making the *r* process is very close to the maximum allowed (not the average neutron star); this raises the gravitational potential, which has the effect of increasing the speed and entropy of the wind (see also Cardall and Fuller, 1997; Otsuki *et al.*, 2000);
(d) important multidimensional effects (clumping?) or general relativistic effects in the neutrino transport have been left out; or
(e) new particle physics, e.g., flavor mixing, might affect Y_e in the wind or its dynamics (Qian *et al.*, 1993; Qian and Fuller, 1995).

In addition to occurring in supernovae, the neutrino wind model for the *r* process has other appealing characteristics. Because it is a wind, the total mass ejected can be small. About $10^{-5} M_\odot$ of *r* process ($A \gtrsim 100$) per supernova would be produced, and this is in good accord with the demands of galactic chemical evolution (Mathews and Cowan, 1990). In addition, since the properties of the wind are determined by the neutron star and not the presupernova star, the *r* process might have very similar properties from event to event for neutron stars of a constant mass. Finally, unless all of the ejected material eventually falls back onto the neutron star (Sec. VI.A), the neutrino wind is an event that must exist in nature. It is doubtful that its nucleosynthetic contribution is negligible, especially for the lighter *r*-process isotopes (e.g., Sr, Y, Zr).

DYNAMICAL r-PROCESS CALCULATIONS

in SN ν-wind require

→ $\sigma(n,\gamma)$ and $R(\gamma,n)$

→ $\sigma(n,\alpha)$, $\sigma(n,p)$

FOR VERY n-rich nuclides

NS+NS and NS+BH MERGERS?

HISTORY : FIRST proposed here by LATTIMER + SCHRAMM (1974

EJECTA : NS+BH

: $\sim 3 \times 10^{-3} M_\odot$ with $Y_e \sim 0.01 \pm 0.05$ as r-process via decompression

: ν-driven wind of the disk $\sim 10^{-4} M_\odot$ with $Y_e \sim 0.1 \pm 0.2$

See JUST et al. 2015, MNRAS 448, 541

Monthly Notices
of the
ROYAL ASTRONOMICAL SOCIETY
MNRAS 448, 541–567 (2015) doi:10.1093/mnras/stv009

Comprehensive nucleosynthesis analysis for ejecta of compact binary mergers

O. Just,[1,2⋆] A. Bauswein,[3] R. Ardevol Pulpillo,[1,4] S. Goriely[5] and H.-T. Janka[1]

[1]*Max-Planck-Institut für Astrophysik, Postfach 1317, D-85741 Garching, Germany*
[2]*Max-Planck/Princeton Center for Plasma Physics (MPPC)*
[3]*Department of Physics, Aristotle University of Thessaloniki, 54124 Thessaloniki, Greece*
[4]*Physik Department, Technische Universität München, James-Franck-Straße 1, D-85748 Garching, Germany*
[5]*Institut d'Astronomie et d'Astrophysique, CP-226, Université Libre de Bruxelles, B-1050 Brussels, Belgium*

Accepted 2014 December 31. Received 2014 November 3; in original form 2014 June 11

ABSTRACT

We present the first comprehensive study of *r*-process element nucleosynthesis in the ejecta of compact binary mergers (CBMs) and their relic black hole (BH)–torus systems. The evolution of the BH–accretion tori is simulated for seconds with a Newtonian hydrodynamics code including viscosity effects, pseudo-Newtonian gravity for rotating BHs, and an energy-dependent two-moment closure scheme for the transport of electron neutrinos and antineutrinos. The investigated cases are guided by relativistic double neutron star (NS–NS) and NS–BH merger models, producing $\sim$3–6 $M_\odot$ BHs with rotation parameters of $A_{\rm BH} \sim 0.8$ and tori of 0.03–0.3 $M_\odot$. Our nucleosynthesis analysis includes the dynamical (prompt) ejecta expelled during the CBM phase and the neutrino and viscously driven outflows of the relic BH–torus systems. While typically $\sim$20–25 per cent of the initial accretion-torus mass are lost by viscously driven outflows, neutrino-powered winds contribute at most another $\sim$1 per cent, but neutrino heating enhances the viscous ejecta significantly. Since BH–torus ejecta possess a wide distribution of electron fractions (0.1–0.6) and entropies, they produce heavy elements from $A \sim 80$ up to the actinides, with relative contributions of $A \gtrsim 130$ nuclei being subdominant and sensitively dependent on BH and torus masses and the exact treatment of shear viscosity. The combined ejecta of CBM and BH–torus phases can reproduce the solar abundances amazingly well for $A \gtrsim 90$. Varying contributions of the torus ejecta might account for observed variations of lighter elements with $40 \leq Z \leq 56$ relative to heavier ones, and a considerable reduction of the prompt ejecta compared to the torus ejecta, e.g. in highly asymmetric NS–BH mergers, might explain the composition of heavy-element deficient stars.

Key words: accretion, accretion discs – hydrodynamics – neutrinos – nuclear reactions, nucleosynthesis, abundances – stars: neutron.

1 INTRODUCTION

Double neutron star (NS–NS) and neutron star–black hole (NS–BH) binaries radiate gravitational waves (GWs) and their orbits shrink due to the associated angular momentum and energy loss until, after millions to hundreds of millions of years, a catastrophic merger event terminates the evolution of these binary systems. The frequency of such events can be estimated on grounds of the known double NS systems in the solar neighbourhood (e.g. Kalogera et al. 2004) and theoretical population synthesis studies (e.g. Belczynski et al. 2008) to be of the order of one NS–NS merger in some 10^5 years for Milky Way-like galaxies and possibly up to several times this rate for NS–BH mergers, but these numbers contain considerable uncertainties (Postnov & Yungelson 2014).

Compact binary mergers are among the most promising extragalactic sources of GWs in the $\lesssim$100 to $\gtrsim$1000 Hz range to be measured by the upcoming advanced interferometer antennas (advLIGO, advVIRGO, and KAGRA). Strong arguments suggest that their remnants are good candidates for the still enigmatic central engines of short gamma-ray bursts (GRBs; see, e.g. Nakar 2007; Berger 2014 for reviews). The merger rate, reduced by the beaming factor measuring the probability that the Earth is hit by the collimated, ultrarelativistic GRB beam, can well account for the number of detected short GRBs.

⋆ E-mail: ojust@mpa-garching.mpg.de

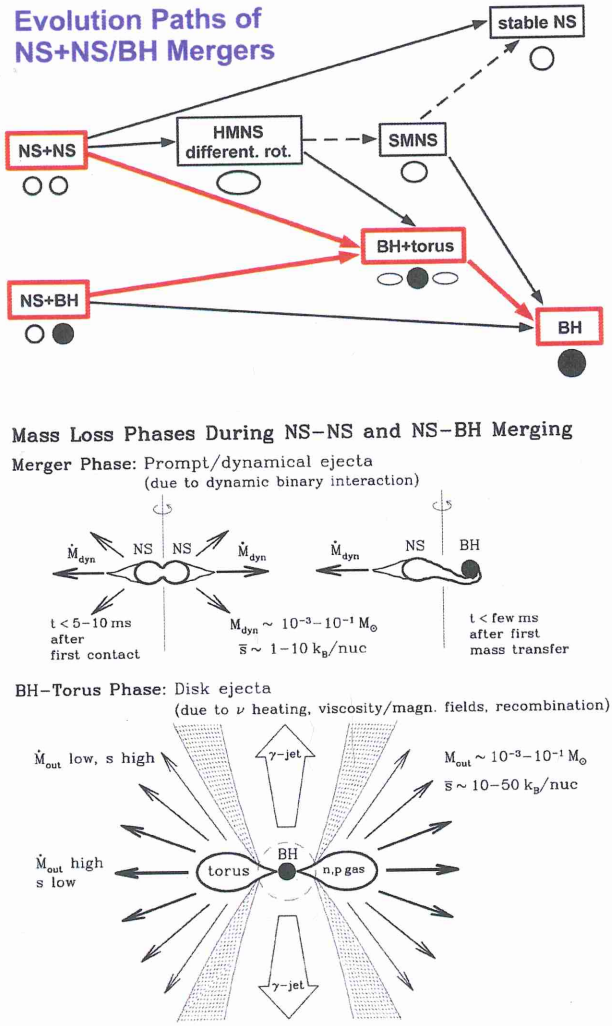

Figure 1. Top panel: evolution paths of NS–NS and NS–BH mergers. Depending on the binary parameters and the properties of the nuclear EOS, binary NS mergers can lead to the formation of a stable NS, a transient HMNS (stabilized by differential rotation) and SMNS (stabilized by rigid rotation), or a BH plus accretion-torus system. The last scenario is also the outcome of a NS–BH merger if the BH/NS mass ratio is not too large. Transitions between the different evolution stages can be accompanied by mass-loss. In this work, we focus exclusively on the evolution tracks and stages highlighted by thick, solid red lines. Bottom panel: mass-loss phases during the dynamical interaction of NS–NS and NS–BH binaries and the subsequent secular evolution of a relic BH–torus system (corresponding to the evolution paths indicated by red lines in the upper panel). The dynamical mass ejection takes place within a few milliseconds when the two binary components merge with each other. Typical ejecta masses are around 0.01 $M_\odot$ and the average entropies of the ejecta are low. BH–torus systems eject matter mainly in viscously driven outflows and to a smaller extent also in neutrino-driven winds. Baryon-poor polar funnels may provide suitable conditions for neutrino or magnetohydrodynamically powered, ultrarelativistic, collimated outflows, which are likely to produce short GRBs. The image is adapted from Ruffert & Janka (1999) and Janka & Ruffert (2002).

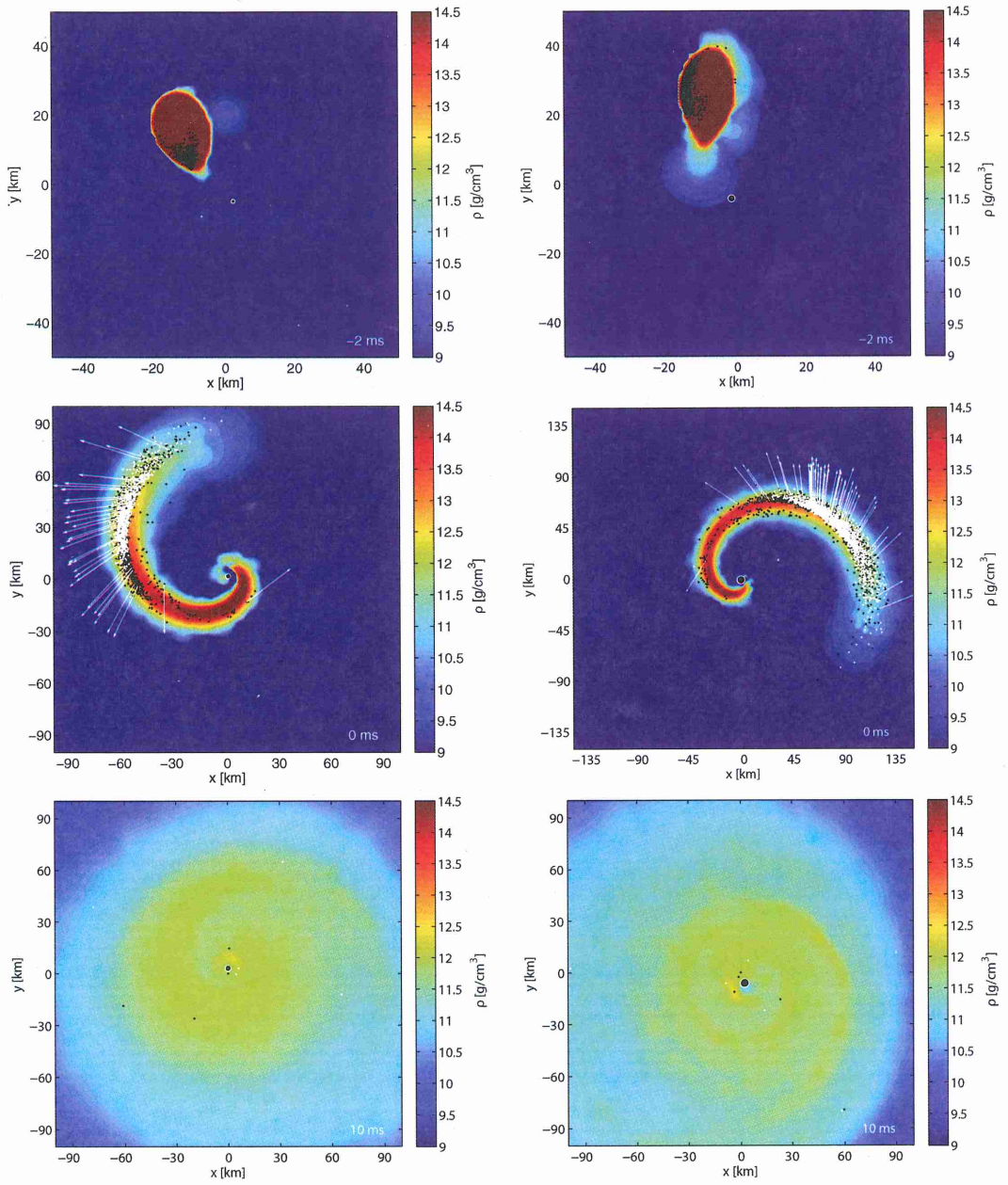

Figure 3. Evolution of the rest-mass density in the equatorial plane for two NS–BH merger models. The left-hand panels correspond to model DD2_14529, which describes the merging of a 1.45 $M_\odot$ NS and a 2.9 $M_\odot$ BH with a spin parameter of 0.53 for the DD2 EOS, the right-hand panels display model TM1_14051, which is the coalescence of a 1.4 $M_\odot$ NS and a 5.1 $M_\odot$ BH with a spin parameter of 0.7 for the TM1 EOS. The time is given in the lower-right corner and is normalized to the moment when the BH has accreted half of the NS matter. The position of the BH is indicated by a filled black circle, whose radius in isotropic coordinates is defined by the gravitational mass of an isolated, non-rotating BH. The dots trace SPH particles (projected into the equatorial plane) which eventually become unbound during the simulations. The white dots denote particles which fulfil the ejecta criterion at the current time, while black dots indicate particles that will only become unbound later on. For a subset of SPH particles the arrows visualize the coordinate velocities of the corresponding fluid elements with the length of the arrows being proportional to the velocity. An arrow length of 10 km corresponds to 0.2 times the speed of light. The visualization tool SPLASH was used to convert SPH data to grid data (Price 2007).

we show in Fig. 4 the properties of the dynamical ejecta in terms of mass-distribution histograms for the electron fraction, entropy per baryon, expansion time-scale and outflow velocity. During the late inspiral phase the NS is tidally deformed and develops a cusp pointing towards the BH. As the star approaches the BH, mass transfer sets in from this cusp and the NS is stretched into an extended, spiral-arm-like tidal tail. While mass is shed off the far end of the tidal arm to expand outwards, the matter at the near end wraps the BH and, if it has sufficiently high angular momentum, performs a full orbit around the BH to collide with the spiral arm. Finally, the

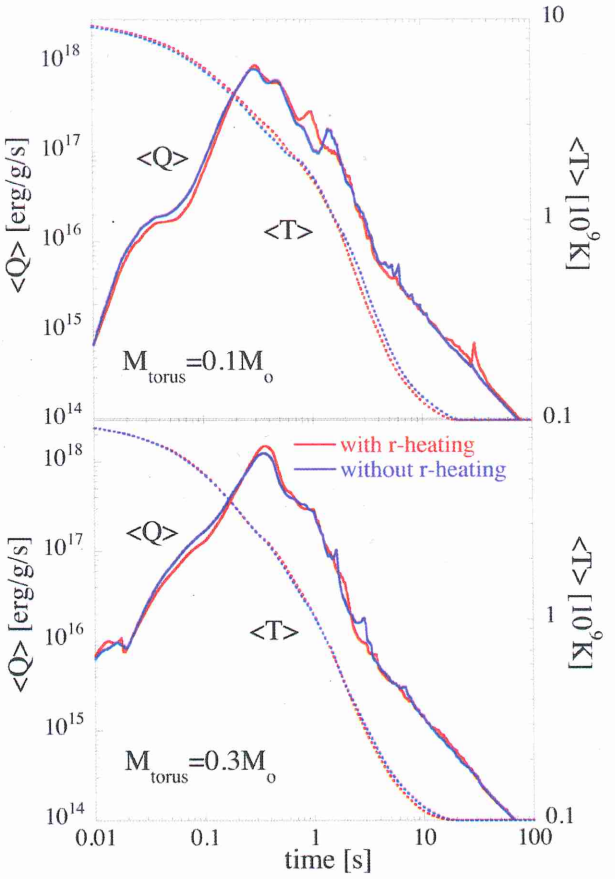

Figure 17. Time evolution of the average radioactive heating rate per unit mass, $\langle \dot{Q} \rangle$, for two BH–torus systems with $M_{\rm BH} = 3\,{\rm M}_\odot$, $A_{\rm BH} = 0.8$, $M_{\rm torus} = 0.1\,{\rm M}_\odot$ (top) and $M_{\rm BH} = 4\,{\rm M}_\odot$, $A_{\rm BH} = 0.8$, $M_{\rm torus} = 0.3\,{\rm M}_\odot$ (bottom), when the heating feedback due to the r-process β-decays and fission is included or not. Calculations correspond to models M3A8m1a2, M3A8m1a2-rh, M4A8m3a5 and M4A8m3a5-rh.

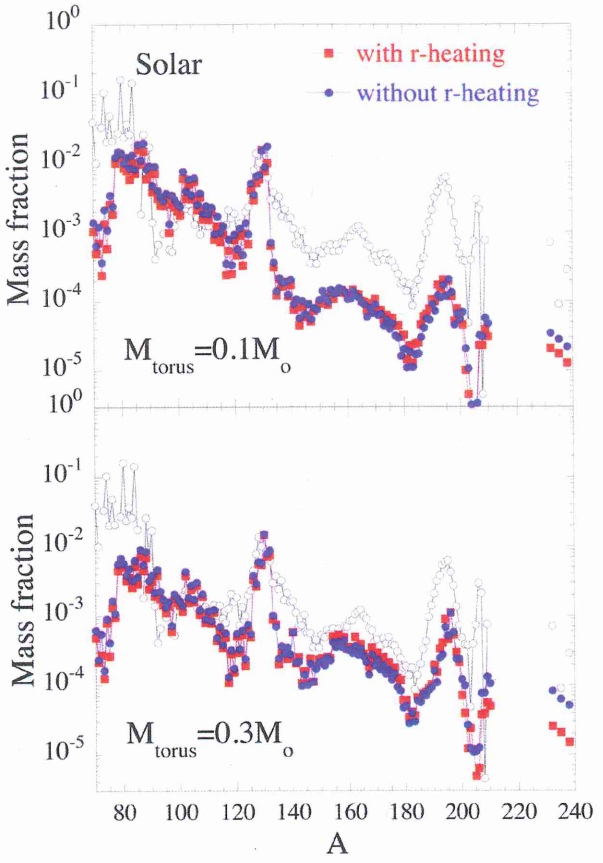

Figure 18. Abundance distributions as functions of the atomic mass for two BH–torus systems with $M_{\rm BH} = 3\,{\rm M}_\odot$, $A_{\rm BH} = 0.8$, $M_{\rm torus} = 0.1\,{\rm M}_\odot$ (top) and $M_{\rm BH} = 4\,{\rm M}_\odot$, $A_{\rm BH} = 0.8$, $M_{\rm torus} = 0.3\,{\rm M}_\odot$ (bottom), when the heating feedback due to the r-process β-decays and fission are included or not. All distributions are normalized to the same solar $A = 130$ abundance. Calculations correspond to models M3A8m1a2, M3A8m1a2-rh, M4A8m3a5 and M4A8m3a5-rh. The dotted circles show the solar r-abundance distribution (Goriely 1999).

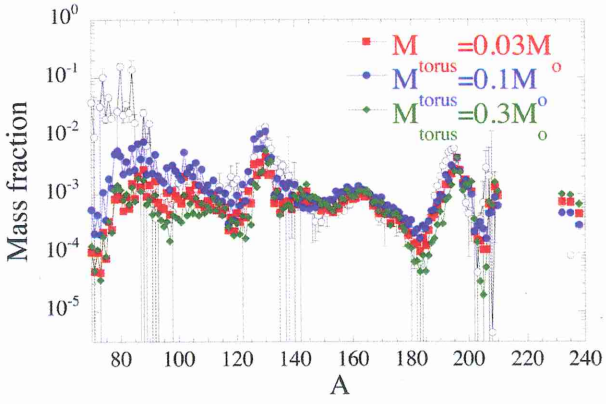

Figure 19. Abundance distributions as functions of the atomic mass for three combined systems (merger model plus remnant model) corresponding to models with torus masses $M_{\rm torus} = 0.03$, 0.1 and $0.3\,{\rm M}_\odot$. All distributions are normalized to the same solar $A = 196$ abundance. Calculations correspond to the model combinations TMA_1616–M3A8m03a5, SFHO_13518–M3A8m1a5 and DD2_14529–M4A8m3a5. The dotted circles show the solar r-abundance distribution (Goriely 1999).

dynamically (both components being composed of about 80–98 per cent of r-process material). For the three cases shown in Fig. 19, this ratio amounts to 1.4, 5.3 and 1.7 for the 0.03, 0.1 and $0.3\,{\rm M}_\odot$ torus models, respectively. For this reason, when normalizing to the $A = 196$ abundance, the lighter elements, and in particular the $A \simeq 130$ peak, are found to typically vary within a factor of 3.

Note that it is well known that calculations of the r-process abundances are still affected by large nuclear physics uncertainties (Arnould, Goriely & Takahashi 2007). Such uncertainties have been extensively studied in the past, but each site provides its specific conditions and behaves in its own special manner so that an assessment of the sensitivity to theoretical nuclear physics input requires careful and dedicated exploration. While we already partly investigated the sensitivity of the nucleosynthesis in the dynamical ejecta to masses, β-decay rates, and fission probabilities (Goriely et al. 2013), we defer such a sensitivity analysis for the composition of the disc ejecta to a future study.

4 COMPARISON WITH OBSERVATIONS

The striking similarity between the solar distribution of r-element abundances in the $56 \leq Z \leq 76$ range and the corresponding abundance pattern observed in ultrametal-poor stars like CS 22892−052

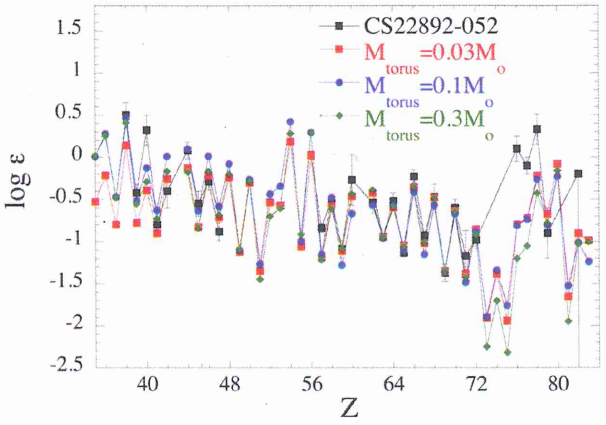

Figure 20. Comparison between the elemental abundances of CS22892-052 (in the usual logarithmic scale relative to hydrogen, $\log\varepsilon = \log_{10}(N_A/N_H) + 12$ for element A and number density N_A) and those obtained for the three combined systems corresponding to remnants with 0.03, 0.1 and 0.3 $M_\odot$ tori as shown in Fig. 19. All distributions are normalized to the observed Eu abundance. Calculations correspond to the model combinations TMA_1616–M3A8m03a5, SFHO_13518–M3A8m1a5 and DD2_14529–M4A8m3a5.

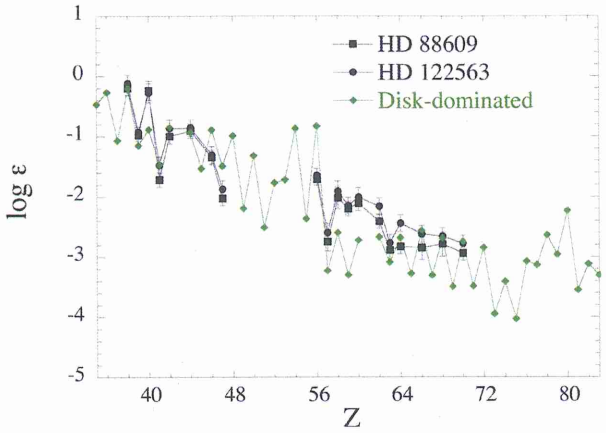

Figure 21. Comparison between the HD 88609 and HD 122563 elemental abundances (in log ε scale) and those estimated for the combination of models SFHO_1123 and M3A8m3a2, when the ejected mass of the dynamical component is assumed to be 100 times smaller than the one coming from the disc component. The calculated distribution is normalized to the Sr abundance of HD 88609.

(Sneden et al. 2003, 2009; Sneden, Cowan & Gallino 2008) led to the conclusion that any astrophysical event producing *r*-elements gives rise to a Solar system *r*-abundance distribution, at least for elements above Ba. In such *r*-process-enriched low-metallicity stars, some variation of about 0.5 dex, however, is found for the elements lighter than Ba. The amazingly robust *r*-process for elements above Ba could point to the possible creation of these elements by fission recycling in dynamical NS–NS or NS–BH merger ejecta, as already argued in previous studies (e.g. Goriely et al. 2011b). As seen in Fig. 19, variations of the abundances of the lighter elements with $40 \leq Z \leq 56$ relative to those of the heavier elements by factors of a few could be accounted for when the contributions of the disc ejecta in dependence on different torus masses are considered. Fig. 20 shows that the elemental distribution observed in the ultrametal-poor star CS22892−052 (Sneden et al. 2003) can be fairly well reproduced by the nucleosynthesis from the combined dynamical and disc ejecta. Discrepancies are found around the Os elements due to the shift of the third *r*-process peak (see Fig. 19), the exact position of which is affected by nuclear uncertainties.

Recent observations also indicate that star to star variations in the *r*-process content of metal-poor globular clusters may be a common, although not ubiquitous, phenomenon (Roederer et al. 2010; Roederer 2011). Stars such as HD 88609 or HD 122563 have been found to be significantly deficient in their heavy elements (Honda et al. 2007). CS 22892−052 and HD 122563 are now interpreted as two extreme cases representative of a continuous range of *r*-process nucleosynthesis patterns (Roederer et al. 2010).

In the previous comparison with CS22892−052, we determined the combined composition of all ejecta components by weighting both the dynamical and disc contributions by their respective total ejected masses. However, it cannot be excluded that the mass of the dynamical ejecta contributing to the final composition is in fact significantly smaller, in particular when considering NS–BH systems. Two different effects could suppress the dynamical ejecta relative to the torus ejecta. (1) As discussed in Section 3.2, the dynamical ejecta of NS–BH mergers can be highly asymmetric, because most of these ejecta may consist of the matter shed off the outer tip of the tidally stretched NS at its final approach to the BH. In contrast, the remnant ejecta are more isotropic. The combination of both can therefore be strongly direction dependent. For the values of the asymmetry parameter B_{asy} given in Table 1 (cf. Section 3.2), the mass of the dynamical ejecta could be 20–100 times smaller than the mass of the disc ejecta outside of the solid angle of the main dynamical mass stripping. (2) Potentially, NS–BH mergers might produce little dynamical ejecta material for certain binary parameters while still forming a torus. This hypothetical possibility might exist in cases where the NS is nearly completely and immediately accreted by the BH, in which case the tidal sling effect leading to mass ejection from an extremely stretched NS might be absent. In such systems, the ejecta would consequently be essentially composed of disc material. If we assume that the contribution of the dynamical ejecta represents only about 1 per cent of the total ejected mass, the composition of the ejecta becomes strongly depleted in heavy *r*-process material in comparison to the standard cases shown in Figs 19 and 20. Such specific system conditions could qualitatively explain the composition of stars like HD 88609 or HD 122563, as shown in Fig. 21. We consider this as an interesting, speculative possibility, but the relative frequency of such possible events as well as the possible variation of the mix between the dynamical and disc contributions will need to be assessed in a more quantitative way in future studies.

5 SUMMARY, DISCUSSION, AND CONCLUSIONS

We have performed the first comprehensive study of *r*-process nucleosynthesis in merging NS–NS and NS–BH binaries, also including the neutrino and viscously driven outflows from BH–torus systems as remnants of the compact star mergers. Our focus was on such relic systems because they are the generic outcome of NS–BH mergers when the BH/NS mass ratio is not too large, and for NS–NS mergers in cases where the massive remnant cannot be stabilized by the NS EOS. We therefore considered binary NSs that either led to BH formation directly when the two stars plunged into each other, or produced a remnant that collapsed to a BH within less than about 10 ms for the nuclear EOSs employed in our work.

THE r-PROCESS

OBSERVATIONAL EVIDENCE

- STANDARD ABUNDANCE DISTR'N
  ≡ SOLAR SYSTEM MATERIAL

  - SEPARATION OF r- FROM s-process NUCLIDES

    - r-process PEAKS AT
      A = 130 & 195, about
      10 mass units below
      s-process 138 & 208 peaks
    - nuclei A > Pb (s-process end)
      (Th, U, ...)

  - NO r-process only elements
    but some close (Eu)

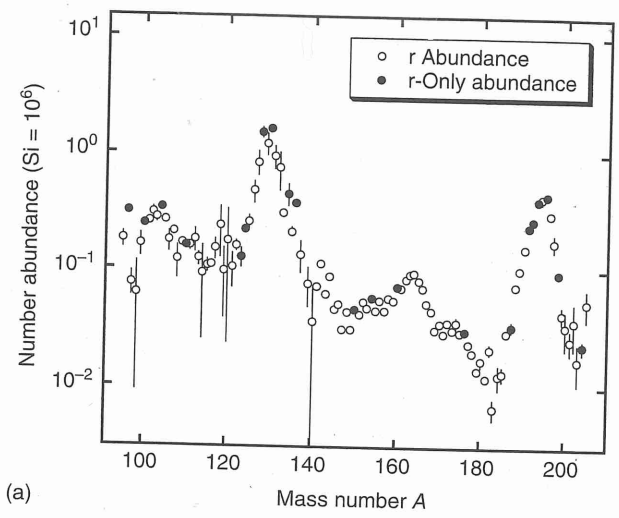

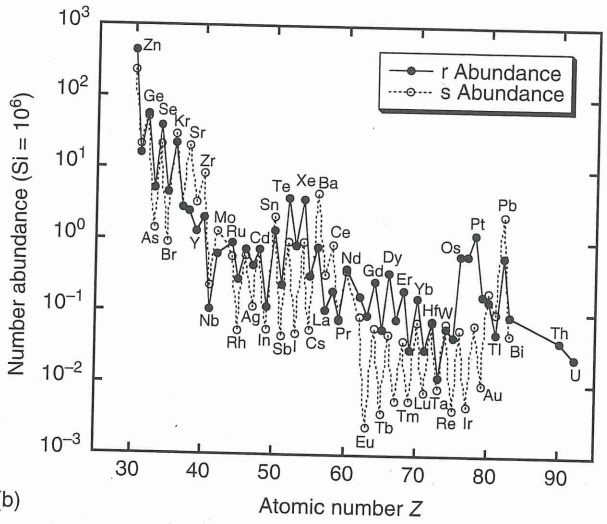

Figure 5.74 (a) Solar system r-process abundances for $A > 90$, obtained by subtracting the s-process contribution from the total solar system abundance. The s-process abundance is calculated by using the classical s-process model (Arlandini *et al.*, 1999). The full circles show abundances of r-only nuclides, defined here as those species for which the s-process contribution amounts to $\leq 3\%$. The influence of the p-process on the displayed abundances is negligible and has been disregarded. The error bars are largest in those regions where the s-process contribution dominates. (b) Elemental solar system s- and r-process abundances. Data from Burris *et al.* (2000).

CLASSICAL DESCRIPTION OF r-PROCESS

B^2FH, ILLINOIS (§6.6.2)

- WAITING POINT APPROX.
- CONSTANT $[T, N(n)]$ for a FIXED time τ and INSTANTANEOUS FREEZE OUT.

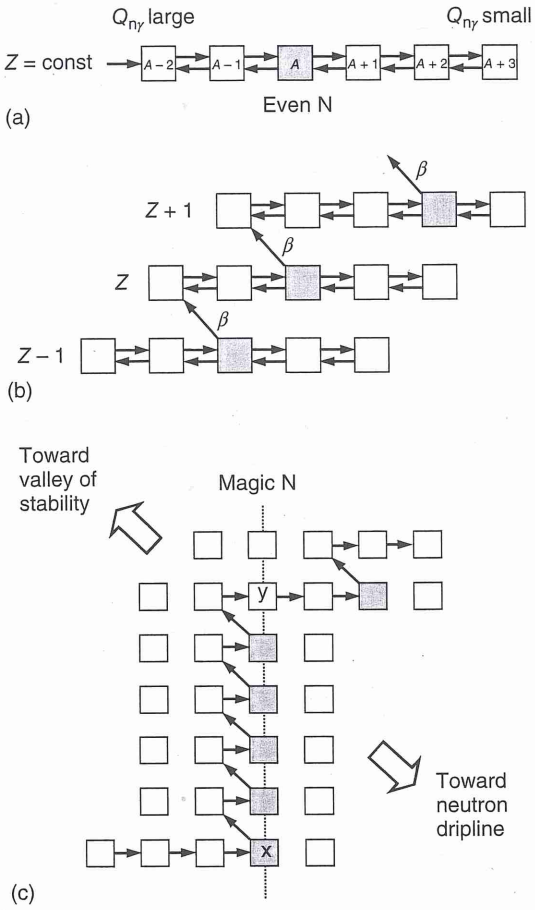

Figure 5.75 Basic building blocks of the r-process path. Part (a) shows an isotopic chain in (n,γ)↔(γ,n) equilibrium (waiting point approximation). For reasons of clarity, it is assumed that most of the abundance resides in a single isotope (shaded square). Part (b) shows how β^--decays of the waiting point nuclides transfer matter from one isotopic chain to the next. The steady flow approximation assumes that the abundance of each element Z is inversely proportional to the total β-decay constant of the chain. Part (c) shows the special case when the r-process path encounters a neutron magic number.

where the symbols have

② Z = constant

$(n,\gamma) \rightleftharpoons (\gamma,n)$ establishes equilibrium ('Saha') abundances for $(T, N(A))$

— need Q-values (masses)
PARTITION FUNCTIONS
λ_β , $\lambda_{\beta\text{-delayed } n}$
FISSION PROPERTIES?

① β DECAYS from N_{max} to near Z chain

③ CLIMB LADDER to MAGIC N NUMBER

CLASSICAL meets SAD

- NO SINGLE SET T, N(n), τ FITS ALL σ
- NEED RANGE

$$T \sim 1.2 - 1.4\ 10^9\ K$$
$$N(n) \sim 3 \times 10^{20} - 3 \times 10^{21}\ cm^{-3}$$
$$\tau \sim 1.5 - 2.5\ mb$$

KRATZ et al. 1993 ApJ 403, 216
2007 ApJ 662, 39

τ_s

— WHERE ARE THE s-PROCESS SITES?

— DYNAMIC rather than CLASSICAL σ-process?

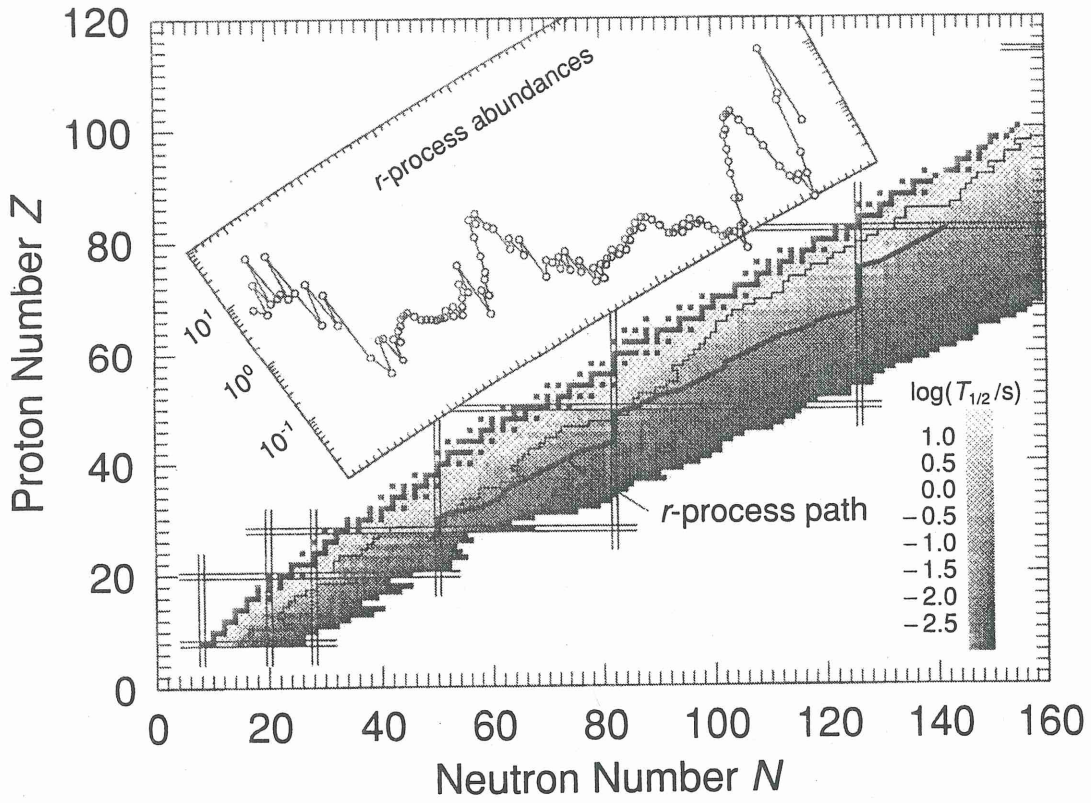

FIG. 1.—Schematic illustration of the *r*-process path (*dark line on neutron-rich side of beta-stability*) and observed *r*-abundances (*inset*). Sharp p
$A \simeq 80$, 130, and 195, where the *r*-process path crosses the $N = 50$, 82, and 126 magic neutron numbers. The chart of neutron-rich nucleides is shac
measured (near stability) and predicted beta-decay half-lives ($T_{1/2}$). Gray scales for $T_{1/2}$ ranges are explained in the legend bar.

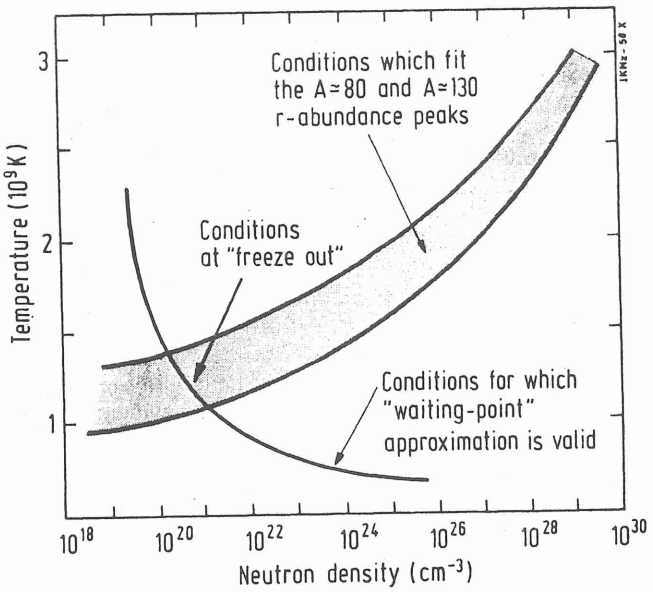

FIG. 4.—Neutron number densities n_n and temperatures T_9 consistent with observed r-process peaks (Käppeler, Beer, & Wisshak 1989) and measured beta-decay rates (Kratz et al. 1988b). Also shown are the conditions found by Cameron, Cowan, & Truran (1983b) for which the classical waiting-point approximation is valid (*beyond solid line*). The thick arrow illustrates temperatures and densities in an r-process environment before freeze-out at $n_n \simeq 10^{20}$ cm^{-3} and $T \simeq 10^9$ K.

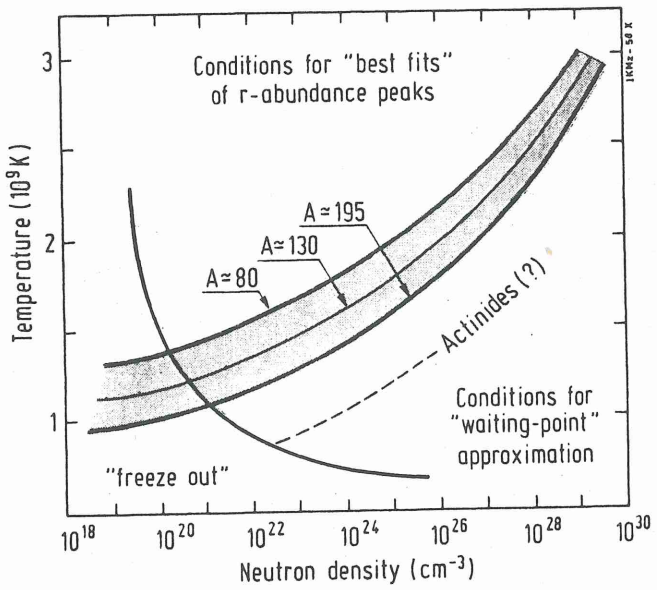

FIG. 12.—Same as Fig. 4, indicating, however, in detail the parts of the n_n-T_9 band which are responsible for different mass ranges of the solar r-process abundance. A superposition of at least three components is required to reproduce the $A \simeq 80$ peak and the two mass ranges $90 \leq A \leq 130$ and $135 \leq A \leq 195$. Because nuclei between Bi and the actinides decay via alpha-decay chains, no clear features emerge for a best fit. The dashed line labeled actinides only indicates a first guess.

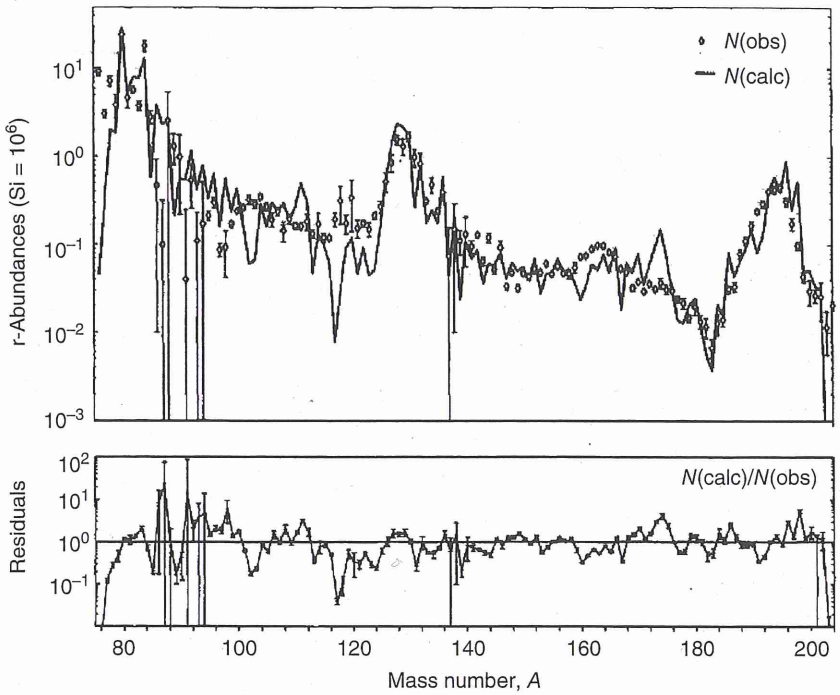

Figure 5.79 Distribution of observed solar system r-abundances (data points) compared to predictions of the classical r-process model (solid line). The solid line is calculated from Eqs. (5.198) and (5.202) and depends only on neutron separation energies, β^--decay half-lives, β-delayed neutron decay probabilities, and so on, but not on cross sections for neutron capture or photodisintegration. The model prediction is obtained from a superposition of three different r-process components. (From Kratz *et al.* (1993). © IOP Publishing. Reproduced by permission of IOP Publishing. All rights reserved.)

a function of neutron density. This procedure requires only a small number of fitting parameters and yields a slight improvement in the predicted r-abundances compared to the results shown in Figure 5.79 (Freiburghaus *et al.*, 1999). However, neither method seems to directly reflect the physical properties of a realistic r-process site.

Figure 5.80 shows some results obtained with the second procedure, that is, by assuming a continuous superposition of r-process components. Each component is characterized by constant values of T, N_n, and τ. The component weights and neutron exposure time scales are given by $\omega(N_n) = a_1 N_n^{a_2}$ and $\tau(N_n) = a_3 N_n^{a_4}$, respectively, where the a_i are fitting parameters. The temperature remains constant at $T = 1.35$ GK. Since different T–N_n conditions correspond to different r-process paths, the overall distribution of waiting point nuclides (large open or solid squares) in each isotopic chain is broadened compared to the use of a single component. The resulting r-process abundance flow pattern represents more appropriately a *boulevard* rather than a narrow path (Kratz, 2006). Nevertheless,

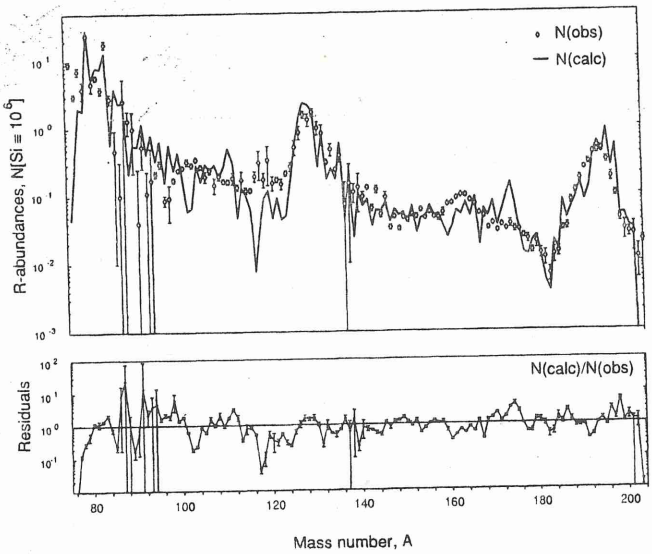

FIG. 17.—Global r-abundance curve obtained from a superposition of three time-dependent calculations with the best-fit n_n-T_9 values for the $A \simeq 80$ peak and the $90 \leq A \leq 130$ and $135 \leq A \leq 195$ mass ranges. The weight of the individual components is 10:2.6:1. In the lower part the ratios of calculated and observed r-abundances are shown. The discussion of the largest deviations at $A = 112$, 115–125, and 176 will be part of § 6.

ODD | INTERESTING!

- N(s) ~ N(r)
  - v. different processes but ~ comparable contributions to SAD
- ~ two s-processes (weak main)
- ~ 'two' r-processes
- Very different & NO INTERMEDIATE neutron-capture processes
- r-process does not run along the neutron drip line [?]

NUCLEAR PHYSICS
—highlights

- THEORY OF r-PROCESS demands nuclear properties of nuclides OFF valley of stability

[EXTRAPOLATION = name of game]

- BEAMS etc. OF RADIOACTIVE NUCLEI probing some n-rich nuclides

EXPERIMENTAL DATA

DO MAGIC NUMBERS STAY UNCHANGED AMONG N-RICH NUCLIDES?

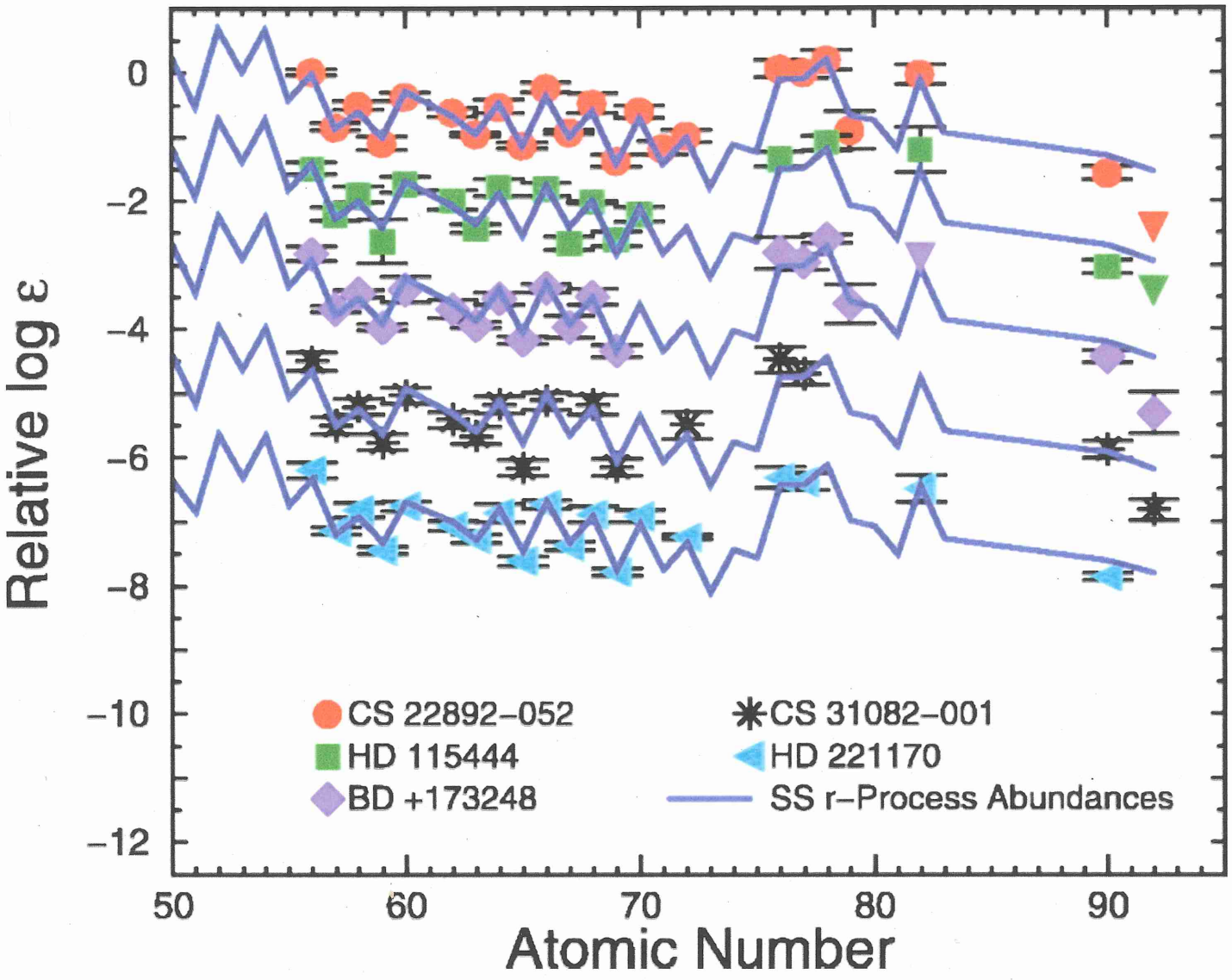
Relative log ε
0
−2
−4
−6
−8
−10
−12
50
60
70
80
90
Atomic Number
CS 22892−052
CS 31082−001
HD 115444
HD 221170
BD +173248
SS r−Process Abundances

- STARS

  – r-process RICH metal-poor halo stars

  ONE r-process for $Z \geq 55$

  + 'weak' r-process for $Z \sim 36$-50

  – STOP PRESS !

  r-process stars in Ret II, ancient dwarf galaxy (UFD)

  "A SINGLE EVENT"

  Ji et al. 2016, Nature, 530, 610

  Roederer et al. 2016, ApJ, 151, 82

  [Fe/H] −2.1 to −3.3

  but [Eu/Fe] ~ +2 in some *s

  and [r/Fe] ~ ⊙ ★

  – r synthesis decoupled from α/Fe

  – r ↓ star is up in Mg

  – one r ★ is rich in C [C/Fe] ≃ 1.1

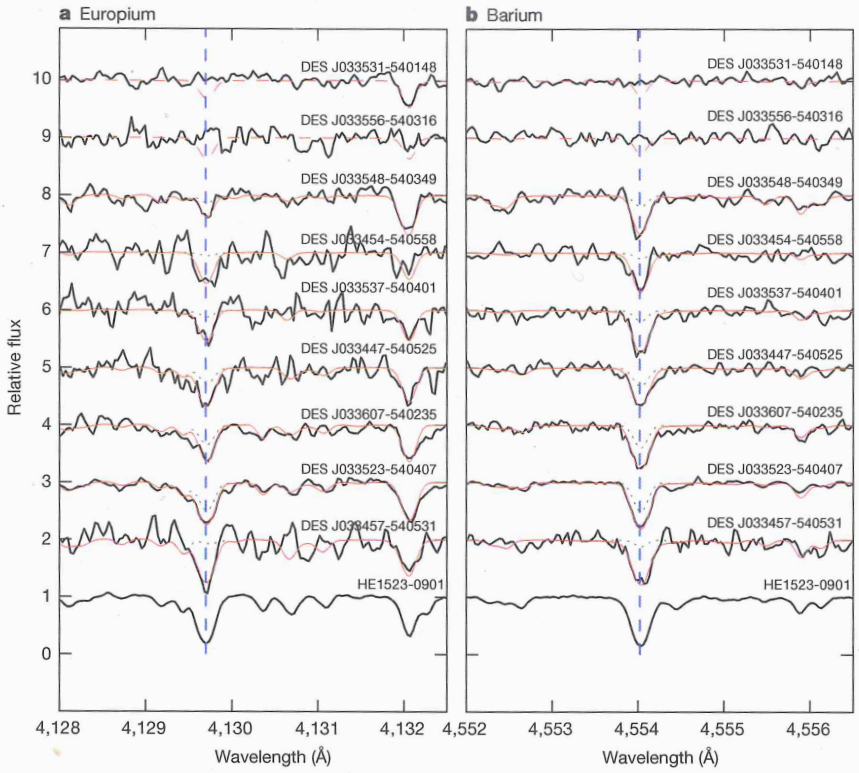

Figure 1 | Spectra of stars in Reticulum II. a, The spectral region around the europium absorption line (412.9 nm) for the nine brightest stars in Reticulum II, identified by the Dark Energy Survey (DES). Absorption is clearly present in seven of the nine Ret II spectra (black lines), including those with modest signal-to-noise ratios. Thin red lines show synthesized fits to the absorption lines (dashed red lines show upper limits). For comparison, dotted green lines show synthesized spectra for each individual star using typical limits found in other UFDs ([Eu/H] = −2.0). Also shown is HE1523-0901, one of the most r-process-enhanced halo stars known[1]. **b**, As for **a**, but showing the region around the barium absorption line (455.4 nm) (the dotted green line shows [Ba/H] = −4.0).

Ji et al.

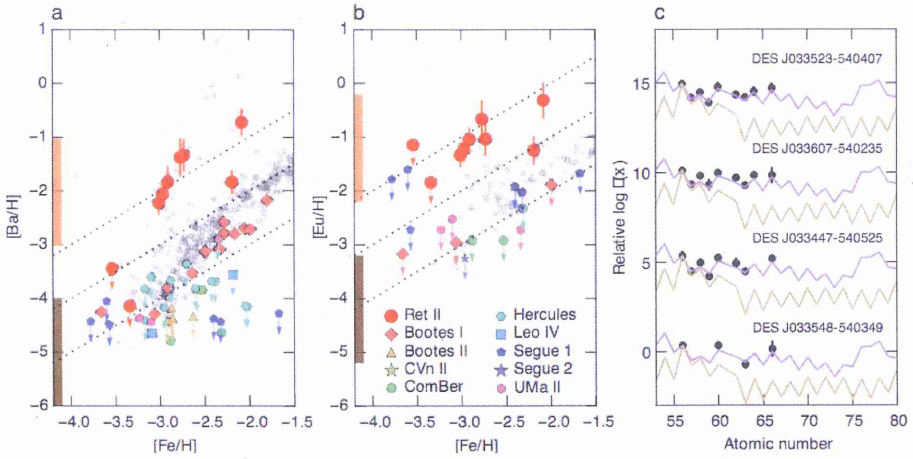

Figure 2 | Chemical abundances of stars in Reticulum II. a, [Ba/H] and [Fe/H] abundances in stars from Ret II (red points), in halo stars[24] (grey points), and in other UFDs (coloured points; see references within refs 16, 17). The orange and brown vertical bars indicate the abundance ranges that would be expected following a neutron star merger and in a core-collapse supernova, respectively. The dotted black lines show constant [Ba/Fe] abundances. Arrows denote upper limits. Error bars represent 1σ (see Extended Data Table 1 and Methods). **b**, As in **a**, but for [Eu/H] abundances. **c**, Abundance patterns beyond barium for the four brightest europium-enhanced stars in Ret II (black dots; see Extended Data Table 2), compared with the solar r-process and s-process patterns[9] (purple and yellow lines, respectively). Solar patterns are scaled to stellar barium abundance. Stars are offset from each other by multiples of five.

Ji et al.

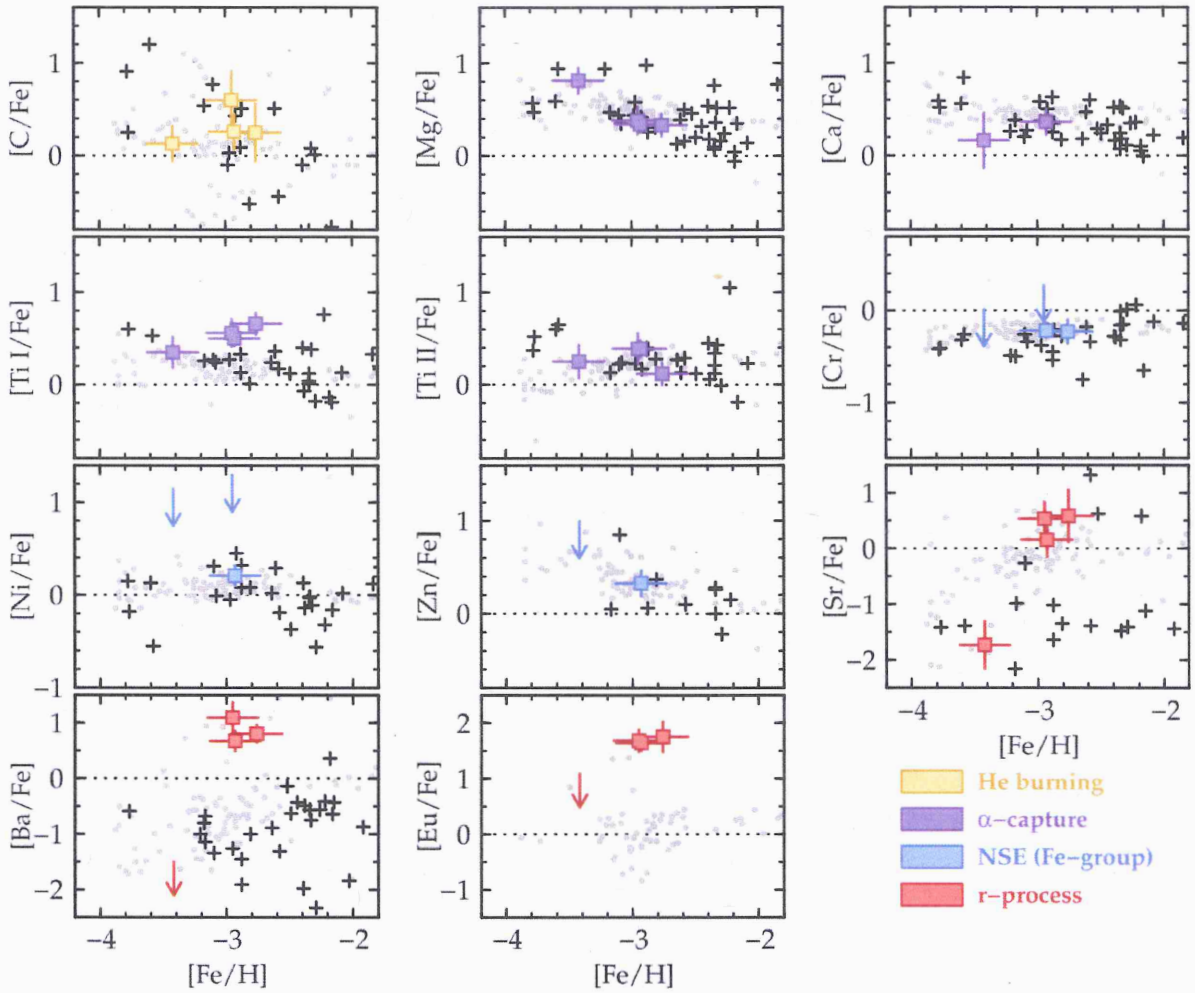

Figure 2. Comparison of abundance ratios in Ret 2 (colored points) with stars in other UFD galaxies (black crosses) and halo giants (gray dots). The UFD sample includes data from Boo I (Feltzing et al. 2009; Norris et al. 2010b; Gilmore et al. 2013; Ishigaki et al. 2014a), Boo II (Koch & Rich 2014; Ji et al. 2015b), CVn II (François et al. 2015), Com (Frebel et al. 2010), Her (Koch et al. 2008, 2013; François et al. 2015), Leo IV (Simon et al. 2010), Seg 1 (Norris et al. 2010a; Frebel et al. 2014), Seg 2 (Roederer & Kirby 2014), and UMa II (Frebel et al. 2010). The halo sample includes only the giants from Roederer et al. (2014b). Upper limits are omitted from the comparison samples for clarity. The colors of the Ret 2 data points indicate the dominant nucleosynthetic origins of each element: yellow, He-burning; green, C and O burning and α-capture in hydrostatic or explosive nucleosynthesis; blue, Fe-group elements formed in nuclear statistical equilibrium (NSE) during explosive nucleosynthesis; red, *r*-process nucleosynthesis. The dotted lines mark the solar ratios. Note the expanded scale on the vertical axes for the [Sr/Fe], [Ba/Fe], and [Eu/Fe] panels.

Roederer et al.

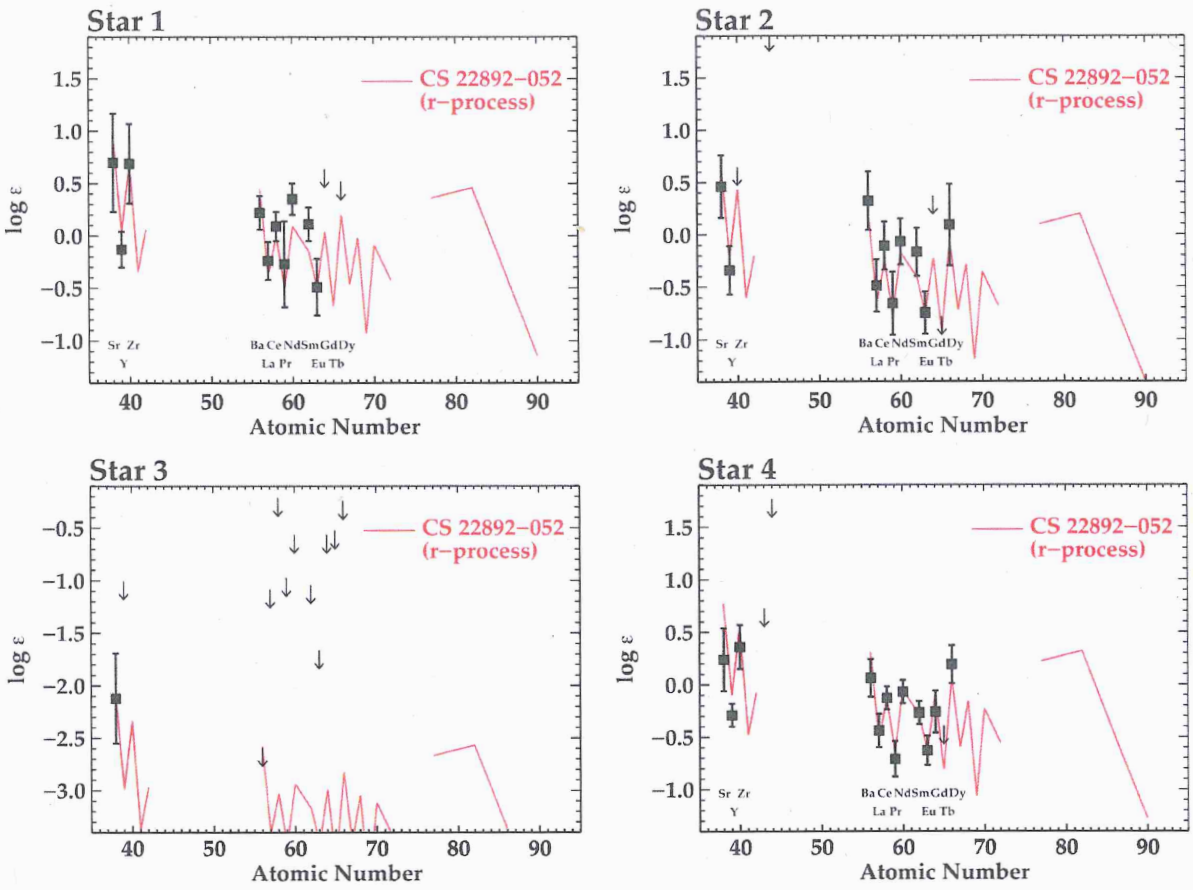

Figure 4. The *n*-capture abundance patterns compared with the *r*-process-enhanced standard star CS 22892–052 (Sneden et al. 2003, 2009; Roederer et al. 2009). The patterns are normalized to Eu ($Z = 63$) in Star 1, Star 2, and Star 4 and to Sr ($Z = 38$) in Star 3. Note the different scale on the vertical axis for Star 3 (lower left panel).

Roederer et al.

BEYOND URANIUM

— AN ISLAND OF BALONIUM.?

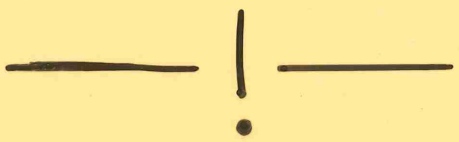

- STABLE ELEMENTS

  H (Z=1) to Bi (Z=83)

  minus Tc (Z=43) and Pm (Z=61)

- NATURALLY OCCURRING HEAVIER ELEMENTS - U, Th decay products

Po	84	
"At"	85	1 oz in Earth's crust
Rn	86	FIRST ALERT detectors
"Fr"	87	<1 oz in Earth's crust
Ra	88	
Ac	89	
Th	90	^{232}Th $\tau_{1/2} \sim 14 \times 10^9$ yrs
Pr	91	few 10^2 gms available from England
U	92	^{238}U $\tau_{1/2} \sim 4.6 \times 10^9$ yrs

ALSO, ^{3}H, ^{14}C from cosmic rays + ...

AND

Pu (Z=94) ^{244}Pu live in early solar system

BEYOND URANIUM

- MANUFACTURE
- NATURALLY OCCURRING?
- ASTROPHYSICALLY RELEVANT?

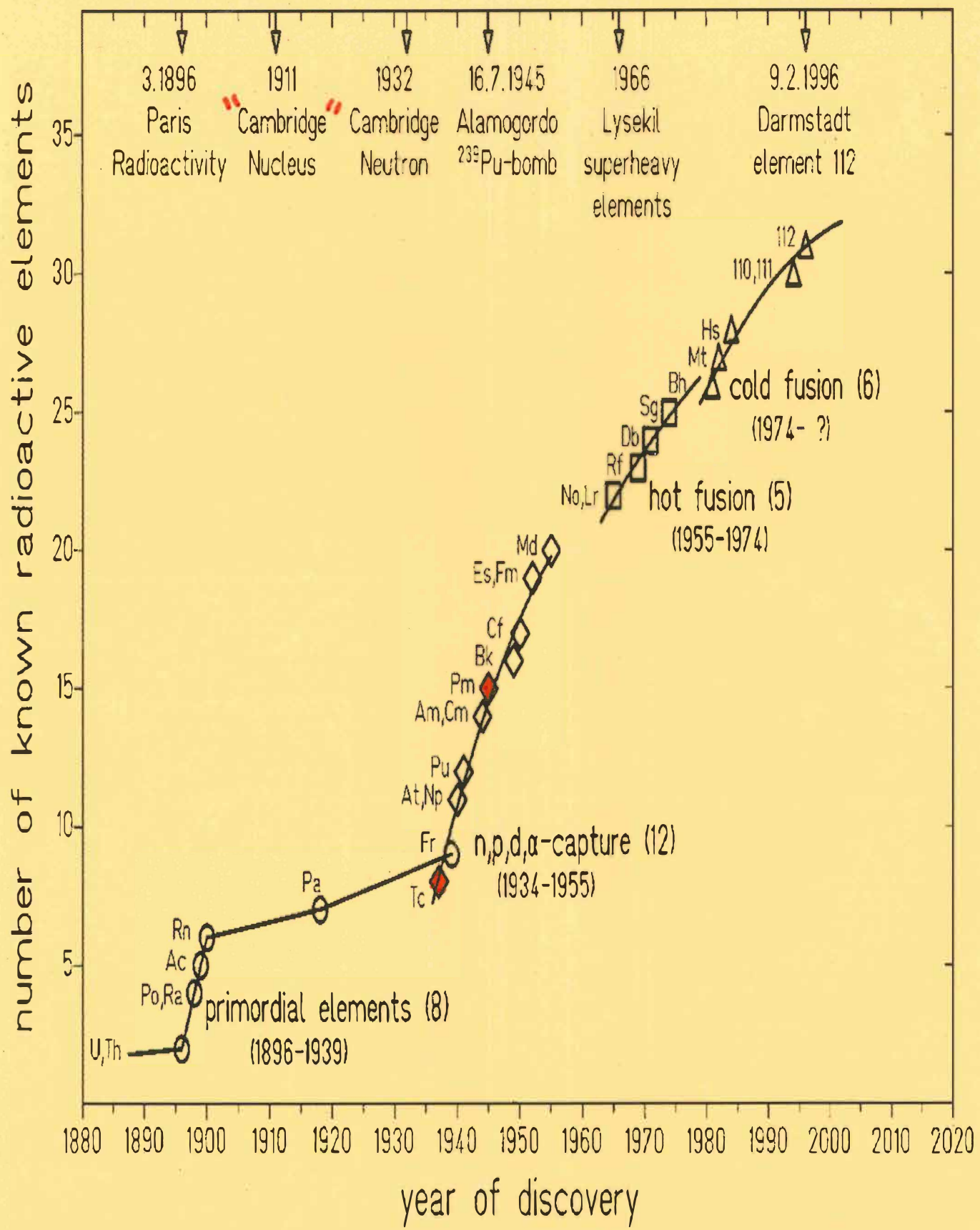
3.1896
Paris
Radioactivity
1911
"Cambridge"
Nucleus
1932
Cambridge
Neutron
16.7.1945
Alamogordo
239Pu-bomb
1966
Lysekil
superheavy
elements
9.2.1996
Darmstadt
element 112
number of known radioactive elements
year of discovery
primordial elements (8)
(1896-1939)
n,p,d,α-capture (12)
(1934-1955)
hot fusion (5)
(1955-1974)
cold fusion (6)
(1974- ?)
U,Th
Po,Ra
Ac
Rn
Pa
Fr
Tc
At,Np
Pu
Am,Cm
Pm
Bk
Cf
Es,Fm
Md
No,Lr
Rf
Db
Sg
Bh
Mt
Hs
110,111
112

- METHODS
  - n, p, d, α capture
  - hot fusion ('hot' ≡ product is excited by 40-50 MeV)

    (B to O) on (Actinide)
  - cold fusion

    (Cr to Zn) + (Pb, Bi, ...)

    CLOSED SHELL NUCLEI

- SMALL σ's: fractions of a pbn ($p \equiv 10^{-12}$)
- LONG BEAM TIMES

  "1 atom per 800 hr of beam time"

SUPERHEAVY ELEMENTS

- SPHERICAL NUCLEI with MAGIC NO.

  $N = 184$, $Z \simeq 120$

  predicted to have long(er) lifetimes

  ISLAND OF STABILITY

- 1969 NILSSON, THOMPSON, TSANG

  predicted $t_{1/2} \sim 10^8 - 10^{10}$ yrs for some SHE ($Z=110$, $N=184$)

  → SEARCHES FOR NATURALLY OCCURRING SHE's OR THEIR DECAY PRODUCTS

  HERRMANN (WELCH CONF. 1990)

- GENTRY et al.

EVIDENCE FOR PRIMORDIAL SHE

Phys. Rev. Lett. 37, 11, 1976

PLEOCHROIC HALOES IN MINERALS

- HALOES from α-DECAY OF U, ..
- GIANT HALOES: imply high E_α and elements > U.
- PROTON-INDUCED X-ray EMISSION

X-ray λ's → Z = 126 'LIVE'

" IF THIS WOULD HOLD FOR BULK MONAZITE IN GENERAL, TONS OF SUPERHEAVY ELEMENTS WOULD LIE AROUND AT SOME BEACHES, e.g. IN INDIA! "

HERRMANN (1990)

BUT BOSCH et al.; WÖLFLI et al. [1976]

(p,n) on Ce → γ-rays

often λ_x due to Sb, Te

- OTHER SEARCHES
  - brine from the Caspian sea
  - old stained (lead) glass windows
  - accelerator beam stops
- NO CONVINCING DETECTIONS!

- IS THERE A SUPERHEAVY ISLAND?
- MANUFACTURE CONTINUES AT
  - LIVERMORE
  - DUBNA
  - DARMSTADT

ASTROPHYSICS

- OLD ^{254}Cf powers Type I SN ?

  1969 COLGATE + MCKEE ^{56}Ni, ^{56}Co

- NEW r- PROCESS

  ALTHOUGH SHE NOT DETECTABLE (DECAY QUICKLY), PRODUCTION AFFECTS Th, U ABUNDANCE

COWAN's CALCULATIONS